Check for updates

Continuous drop-in-biofuel production from pretreated sugarcane bagasse in a microwave-visible irradiated continuous stirred slurry reactor: reaction kinetics & techno-enviro-economic sustainability analyses†

Sourav Barman and Rajat Chakraborty [ID] *

This work utilizes an innovative microwave-visible irradiated continuous stirred slurry reactor (MWVIS-CSSR) for sustainable continuous production of a drop-in biofuel, namely, ethyl levulinate (EL), from pretreated sugarcane bagasse (PSCB). Besides, a novel realistic kinetic model, considering MWVIS intensified EL production through parallel non-catalytic and homogeneous–heterogeneous catalytic pathways in the presence of a magnetic $Ni_{0.5}Zn_{0.5}Fe_2O_4$ (NZF) photocatalyst in conjunction with an oxalic acid–choline chloride based acidic deep eutectic solvent (DES2), was also formulated and validated (R^2 adj. ≥ 0.95). The 5 liter volume MWVIS-CSSR could render maximum 54.7 mol% EL yield (selectivity: 97.85%) at a feed flow rate of 35 ml min^{-1} under optimized conditions (temperature: 100 °C, NZF loading: 6 wt% PSCB, stirring speed: 500 rpm). Remarkably, the synergistic impact of MW and VIS irradiation substantially elevated the EL yield (54.7 mol%) compared to those of the individual MW (29.45 mol%) and VIS (20.1 mol%) systems. The optimally produced EL when blended at 5 vol% with B10 and B20 (10% and 20% biodiesel–diesel blends) could enhance the brake thermal efficiency (1–2%) besides mitigating 21–22% HC and 7.5–20% CO engine exhaust emissions in comparison with reference blends (B10 and B20). Notably, the reactor scale-up study based on the penetration depth of the MW and VIS energy of NZF and DES2 showcased the potential to upscale the 5 liter MWVIS-CSSR to a 1 m^3 volume, allowing EL production to reach 689 kg h^{-1} with a sugarcane bagasse processing capacity of 2000 kg h^{-1}. Moreover, the process simulation conducted in Aspen Plus software, utilizing COSMO-based property estimation with DFT calculations, alongside the techno-economic analysis, revealed a robust internal rate of return (IRR) of 54.25% and a net present value (NPV) of 8.22×10^5 US$ with a payback period of 4.91 years. Additionally, the environmental impact analysis study for the scaled-up EL production process in the MWVIS-CSSR revealed a reduction of 40–60% in marine ecotoxicity and 39–61% in human toxicity compared to the separate MW-CSSR and VIS-CSSR systems.

Sustainability spotlight

Ethyl levulinate (EL) is a potential oxygenated drop-in biofuel and a versatile platform chemical. Hence, with sustainable production of EL from lignocellulosic biomass, EL is set to have a promising future as a central platform chemical within the developing biorefinery sector. This work offers an energy-efficient, sustainable method for continuous EL production using a microwave-visible irradiated slurry reactor with a magnetic $Ni_{0.5}Zn_{0.5}Fe_2O_4$ photocatalyst and an oxalic acid–choline chloride deep-eutectic-solvent. The developed realistic EL production kinetic model in this work could aid in efficient reactor design for industrial scale-up. Additionally, the study assessed the economic feasibility, environmental impacts of the continuous EL production process, and engine performance of EL blended fuels, highlighting EL's potential in reducing emissions. This work aligns with UN SDG 7 (affordable and clean energy), SDG 9 (industry, innovation, and infrastructure), and SDG 13 (climate action).

1 Introduction

In a rapidly developing country like India, rising air pollution from transportation is a major concern. In this respect, the Central Pollution Control Board under the Ministry of Environment, Forest and Climate Change, Government of India

Chemical Engineering Department, Jadavpur University, Kolkata-700032, India. E-mail: rajat_chakraborty25@yahoo.com; rajat.chakraborty@jadavpuruniversity.in; Tel: +91 3324572689

(GOI) introduced Bharat stage VI emission standards (BS-VI) norms in 2020 to regulate the vehicle exhaust emissions.[1] In order to meet such stringent emission regulations, biodiesel has been blended with commercial diesel to upgrade exhaust emission quality.[2] However, biodiesel also has some shortfalls, *viz.* high viscosity and cloud point and low volatility, which have plagued the use of biodiesel in cold climates.[3] Ethyl levulinate (EL), a potential oxygenated drop-in biofuel (oxygen content: 33%) for biodiesel, has recently gained popularity as a cold flow enhancer.[4] Unlu *et al.*[5] reported that 20 vol% blending of EL with canola oil biodiesel could significantly enhance the kinematic viscosity (3.5 mm^2 s^{-1}) and cloud point (-6 °C) properties of the blended fuel. Besides serving as a cold flow enhancer, EL serves as a versatile platform chemical for the production of high-value compounds, including 2-methyltetrahydrofuran, γ-valerolactone, valeric esters and more.[6-8] Hence, with sustainable production of EL from lignocellulosic biomass, EL is set to have a promising future as a central platform chemical within the developing biorefinery sector.

In the literature, various studies investigated the EL synthesis process from lignocellulosic biomass as well as cellulose-derived platform chemicals such as glucose, HMF, furfural and levulinic acid, employing both homogeneous and heterogeneous catalysts.[9] Among homogeneous catalysts, acidic ionic liquids and DESs have been recently employed as promising homogeneous catalysts for EL synthesis from biomass, owing to their high thermal stability and non-toxicity compared to strong mineral acids. For instance, Guan *et al.* employed a sulfonated ionic liquid (IL) and managed to attain a 16 wt% yield of EL from wheat straw within 60 minutes at a temperature of 200 °C.[10] On the other hand, Sert *et al.*[11] achieved 86.83 mol% EL yield from levulinic acid by utilizing a choline chloride–*p*-toluene sulfonic acid-based DES at 90 °C for the same time duration. Other work done by Hu *et al.* achieved 88.82 mol% EL yield from furfuryl alcohol by utilizing ChCl-5-sulfosalicylic acid (5-SSA) based acidic DESs at 100 °C and 2 h.[12] It's worth noting that there has been substantial research into the direct conversion of EL from lignocellulosic biomass using ionic liquids. However, there currently exists a research gap in the direct transformation of EL from lignocellulosic biomass or cellulose using DESs, despite the advantages of DESs over ILs, including their cost-effectiveness, straightforward preparation, and reduced toxicity.
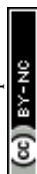
In recent decades, researchers have demonstrated that substituting conventional heating with microwave heating significantly amplifies reaction rates. For instance, Nguyen *et al.* reported that MW heating outperforms conventional heating methods and demonstrated that, through MW irradiation, it is possible to achieve 90.38% EL from levulinic acid (LA) within 60 minutes at a temperature of 200 °C under non-catalytic conditions.[13] Liu *et al.*[14] demonstrated that mechanically pretreated corn stover produced 31.23% EL at 160 °C under MW irradiation (power: 600 watt). Other electromagnetic radiations mainly UV and visible (VIS) light were also employed to synthesise EL through photocatalytic esterification of LA. Raut *et al.* produced 94 mol% EL from levulinic acid employing a carboxylic acid functionalized IL entangled porphyrin photo-catalyst under 5

watt LED light at room temperature for 20 h.[15] Another study done by Castañeda *et al.* reported that a fluorine (1%) modified TiO$_2$ photocatalyst successfully converted 100% of LA to EL in the presence of CCl$_4$ solvent in 1 h at 60 °C under UV irradiation.[16] It is noteworthy that, so far, no research has been reported on the synthesis of EL from lignocellulosic biomass using a photocatalyst, primarily due to challenges associated with the separation of the nano-photocatalyst from the reaction mixture. Magnetic Ni–Zn–ferrites (NZF) have drawn significant research attention for their distinctive electric and magnetic properties, high stability, and lower energy bandgap, rendering them suitable as magnetically separable visible range photocatalysts for various photochemical reactions.[17,18] Work done by Nimisha *et al.*[19] showed that 88% fluorescein dye degradation could be achieved employing NZF under solar irradiation in 1 h.

Very recently, our research group demonstrated the synergistic enhancement of reaction rates by combining different electromagnetic radiations, resulting in energy savings compared to conventional heating methods.[20,21] In a study conducted by our group,[21] it was found that employing microwave-xenon irradiation yielded a 60.3 mol% EL yield from delignified sugarcane bagasse in the presence of a ternary DES composed of FeCl$_3$, citric acid, and choline chloride. Notably, there has been no reported research on EL synthesis using NZF photocatalysts and DESs through the effective utilization of microwave-visible irradiation.

Regarding choosing lignocellulosic biomass for EL production, sugarcane bagasse has emerged as a prime candidate owing to its widespread availability as an agro-industrial residue, particularly in countries like India, where it accounts for approximately 23% of global sugarcane production.[22] Moreover, its relatively high cellulose and hemicellulose content makes sugarcane bagasse a favourable feedstock for the EL production process.

Some works have been reported on continuous flow reactor systems, *viz.* fixed bed reactors, pervaporation membrane reactors, and reactive distillation for synthesis of EL from LA.[23] For instance, Unlu *et al.*[24] reported that 100% LA conversion had been realised in 5 h at 70 °C within a pervaporation membrane reactor using a silicotungstic acid functionalized membrane. Kong *et al.*[25] used a catalytic fixed-bed reactor filled with cerium-phosphotungstic acid grafted silica gel pellets for EL synthesis and reported that 99.0% EL yield was accomplished in 50 h. Notably, a fixed bed reactor encounters certain key challenges, *viz.* non-uniform heat transfer and high pressure drop across the reactor bed, whereas a membrane reactor has high initial costs.[26] Nevertheless, raw lignocellulosic biomass presents a notable challenge due to its inherent difficulty in solubilization with solvents. In previous studies, researchers addressed this issue by employing a two-step process where intermediate levulinic acid was used to generate ethyl levulinate in a continuous reactor. In the context of continuous EL synthesis from lignocellulosic biomass, a continuous stirred slurry reactor (CSSR) could stand out in its ability to maintain consistent mixing and temperature control when dealing with slurry feeds, outperforming other reactor types. Notably, Bermúdez *et al.*[27] emphasized the necessity of taking into account a significant
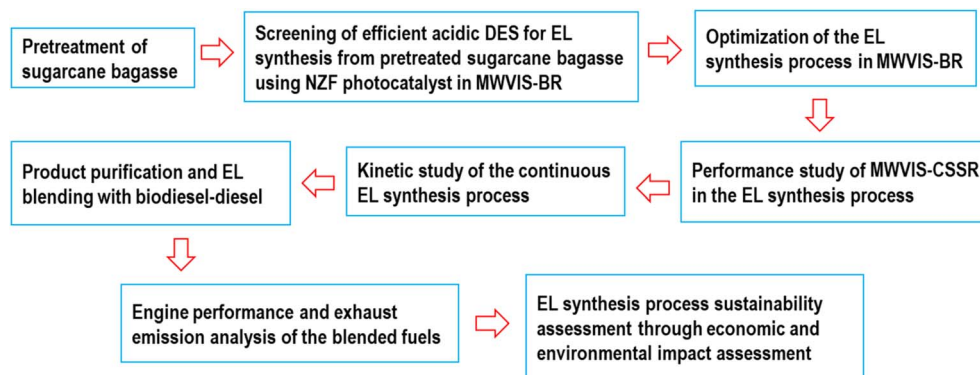
Fig. 1 Sequential steps of the present work.

amount of reaction mass for a precise assessment of the true energy efficiency of the MW irradiation system. Therefore, in this study, to attain a thorough comprehension of both the actual energy performance of the MW-VIS irradiation system and the sustainability of the process, the EL synthesis process was conducted in a sizable continuous flow stirred slurry reactor, following prior batch system experimentation.

Kinetic studies conducted on lignocellulosic biomass to EL synthesis processes have so far extensively employed simplified pseudo-homogeneous kinetic models to describe such multiphase reactions.[28,29] For instance, Tao *et al.*[30] employed a simplified pseudo-homogeneous first order kinetic model to understand the EL synthesis process from cellulose in the presence of a solid $Al_{2/3}H_2SiW_{12}O_{40}$ catalyst. However, development of a realistic reaction kinetic model for such complex multiphase reactions is crucial to understanding the reaction mechanisms and scaling up industrial processes. As far as we know, no scientific literature is available on the development of a kinetic model by considering the PSCB to EL conversion through a parallel homogeneous–heterogeneous reaction pathway in the presence of an NZF photocatalyst and acidic DES.

In recent years, a number of studies have examined the engine performance of EL as a fuel additive in a biodiesel–diesel blend. For instance, Wang *et al.* investigated the four-stroke diesel engine performance of an EL–diesel blend, and reported that smoke emission decreased with increasing EL content.[31] Notably, Lei *et al.*[32] optimized the ethyl levulinate–biodiesel–diesel blends based on the blended fuel's physical and chemical properties. This research also entailed an analysis of the performance and exhaust emissions resulting from the utilization of these optimized blended fuels in a diesel engine. However, it is noteworthy that there is a gap in the existing literature as no prior work has been reported regarding the optimization of EL blending ratios with biodiesel–diesel fuel blends, with a particular focus on the exhaust emissions and the associated environmental impacts of these blended fuels.

Computational resources nowadays play a crucial role in the successful design and assessment of overall process sustainability in biorefineries. This involves a comprehensive analysis of process economics and associated environmental impacts.

Aspen Plus software is extensively employed to seamlessly scale up laboratory-scale processes to industrial operations, facilitating detailed economic evaluations for informed and cost-effective decision-making.[33] Concurrently, in recent years, environmental impact analysis has become an essential technique for assessing climate change risks, examining a process's environmental effects, and scrutinizing energy consumption. Cañon *et al.* investigated the overall process sustainability of EL production from Colombian rice straw, utilizing both Aspen Plus and OpenLCA software.[34] In the present work, we have also made an effort to investigate the overall sustainability of the continuous EL synthesis process through economic and environmental impact analysis employing both Aspen Plus and OpenLCA software.

So, the primary objective of the current work was to produce EL synthesis from sugarcane bagasse (SCB) through a sustainable and energy efficient protocol. To achieve this, various acidic DESs were initially prepared, and their efficacy in EL synthesis was investigated (Fig. 1) in the presence of the NZF photocatalyst under the photo-thermal effect of MW and VIS irradiation systems within a batch reactor (MWVIS-BR). Subsequently, the batch EL production process parameters were optimized. Following this, the EL synthesis process was explored within a continuous stirred slurry reactor system (MWVIS-CSSR), and continuous EL synthesis kinetic analysis was performed. The produced EL was blended with biodiesel–diesel, and its impact on fuel properties, engine performance, and exhaust emissions was analysed, alongside determining the optimal EL blending ratio through environmental impact assessment. Finally, the entire SCB to EL conversion process was upscaled to handle a processing capacity of 2000 kg h^{-1} of SCB and simulated using Aspen Plus, followed by a comprehensive sustainability assessment involving economic and environmental impact analyses.

2   Materials and methods

2.1.   Materials

Ethanol (99.9%), choline chloride (ChCl, 98%), *p*-toluene sulfonic acid ($CH_3C_6H_4SO_3H \cdot H_2O$), oxalic acid ($C_2H_2O_4 \cdot 2H_2O$), malonic acid ($CH_2(COOH)_2$), citric acid ($C_6H_8O_7 \cdot H_2O$),

phenylpropionic acid ($C_9H_{10}O_2$), ethyl levulinate (EL), levulinic acid, 5-ethoxy methyl furfural (5EMF), ethyl β-D-glucopyranoside, ethyl β-D-xylopyranoside, peroxyacetic acid, and NaOH were purchased from Merck. Ni–Zn–ferrite (NZF) nanoparticles ($Ni_{0.5}Zn_{0.5}Fe_2O_4$; size <30 nm) were procured from Nanoshel Limited whereas sugarcane bagasse (SCB) was collected from Shree Renuka Sugars Limited, Haldia, India.

2.2. Methods

2.2.1. Screening of DESs for efficient EL synthesis.
To assess the efficacy of acidic DESs in the efficient synthesis of EL from pretreated sugarcane bagasse (PSCB) (the detailed pretreatment process is given in ESI Section S1†), five acidic DESs with a broad pH range were synthesized. The DESs were prepared by combining choline chloride (ChCl) with p-toluene sulfonic acid, oxalic acid, malonic acid, citric acid, and phenylpropionic acid in a 1 : 1 molar ratio, as specified in Table 1 and subsequently employed in the EL synthesis process.

The batch EL synthesis process (Fig. 2(a)) was performed in an MW (frequency: 915 MHz; specific power input: 4 watt per ml of reaction volume)-VIS (wavelength: 400–700 nm; specific power input: 4 watt per ml of reaction volume) irradiated stirred batch reactor (MWVIS-BR) at fixed reaction conditions (temperature: 100 °C, time: 45 min; stirring speed: 500 rpm) in the presence of the NZF photocatalyst. In this arrangement, 1 g of PSCB was reacted with 10 ml of ethanol in the presence of a fixed amount of the prepared DES and NZF nano-photocatalyst (5 ml of DES and 4 wt% NZF, proportional to the PSCB quantity).

2.2.2. Optimization of EL synthesis process in the MWVIS-BR.
After identifying the most effective DES, the optimization of other process factors associated with the EL synthesis process, viz. temperature (Ω_T), stirring speed (Ω_S), NZF to PSCB ratio ($\Omega_{NZF/PSCB}$) and synthesis time (Ω_t) (Table 2), was carried out. For this object, L-9 Taguchi orthogonal design (L9-TOD) was employed to design experimental runs at different factorial combinations, as outlined in Table 3 and a total nine experimental runs were conducted. Notably, the levels of the four process factors were chosen according to the preliminary results obtained from the single factorial experimental studies. After completion of nine experimental runs, the optimum factorial levels for the EL synthesis process in the MWVIS-BR were determined through SN ratios (eqn (1)) while considering the "larger is better" option for EL yield (Ω_{EL}) as the response parameter. The Ω_{EL} (mol%) was calculated according to eqn (2)

$$\text{SN ratio} = -10 \log \left(\frac{1}{n} \sum_{i=1}^{n} \frac{1}{\Omega_{EL}^2} \right) \quad (1)$$

$$\Omega_{EL}(\text{mol\%}) = \frac{\text{g of EL produced}}{(\text{g of holocellulose present in DSB} \times 0.8891)} \times 100\% \quad (2)$$

Here, i is the number of replications and n the number of experimental runs as per L9-TOD. The denominating factor 0.8891 accounts for the mass reduction during conversion of the repeating units of holocellulose (hemicellulose + cellulose) present in PSCB to EL.

2.2.3. Product analysis.
After completion of the EL synthesis process from pretreated sugarcane bagasse, the reaction mixture was separated according to Fig. S1.† After separation, the EL and by-products were purified using a syringe filter before the analysis. The analysis of the EL and byproducts such as ethyl formate (EF), 5-ethoxymethyl furfural (5EMF), 5-hydroxymethyl furfural (5HMF), and ethyl glycopyranosides (EDGP) was performed using GC-MS with an HP-5MS column (0.25×30 m^2), with helium serving as the carrier gas at a flow rate of 1.0 ml min^{-1}. The samples were injected at a volume of 1 ml with a split ratio of 1 : 10, while maintaining the inlet and source temperatures at 250 °C and 280 °C, respectively.

The other intermediate products (glucose, oligosaccharides) were analysed using HPLC (Waters high performance carbohydrate column: P/N WAT044355: 4.6 mm × 250 mm column with 4 μm Nova-Pack@ spherical silica bonded with trifunctional amino propyl silane; Waters 410 refractive index (RI) detector). Acetonitrile and water (75 : 25 (V/V)) with a flow rate of 1.4 ml min^{-1} were used as a mobile phase.

2.2.4. EL synthesis in MWVIS-CSSR.
After the optimization study in the MWVIS-BR, the performance of a large MWVIS assisted continuous-stirred slurry reactor, i.e. MWVIS-CSSR (reactor diameter: 15 cm; reactors height: 30 cm; with a total working volume of 5 L), in the EL synthesis process was investigated to assess the intensification effects of MW and VIS energy in the presence of large reaction volume. The decision to use a CSSR or over a plug flow reactor was driven by the aim to achieve a homogeneous slurry, a characteristic challenging to attain in plug flow systems due to superior reactant mixing and uniform reaction conditions. As shown in Fig. 2(b), PSCB and NZF were first fed to a mixing tank through a screw feeder, where they were mixed with the DES. The resultant mixed slurry was then fed to the MWVIS-CSSR through a diaphragm pump

Table 1 Components, freezing point, and pH of different prepared acidic deep eutectic solvents

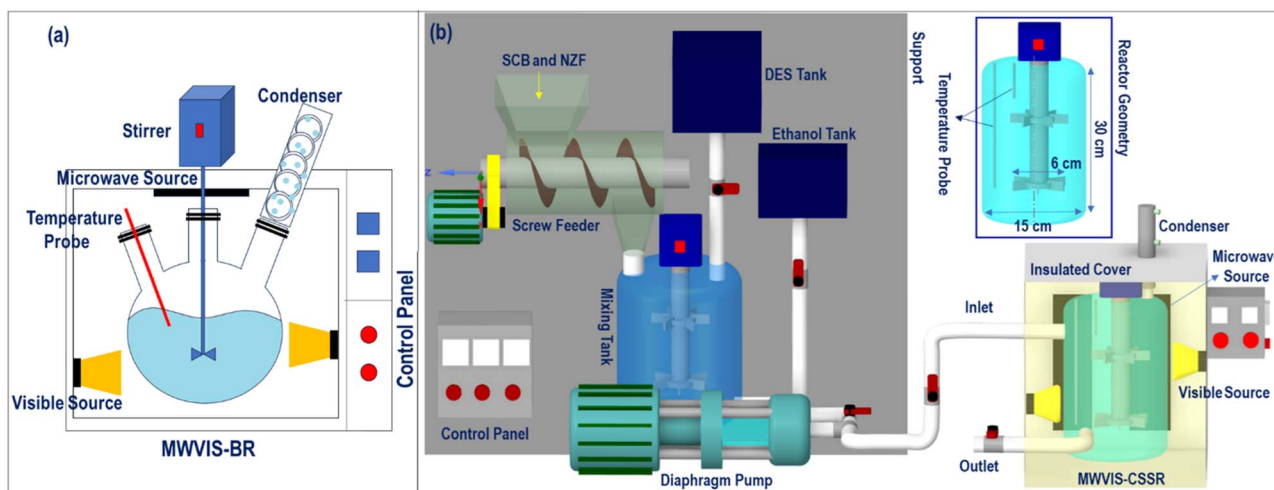| Abbreviation	DES	Freezing temperature (°C)	pH (at 25 °C)
DES1	Choline chloride : p-toluene sulfonic acid	12	−1.45
DES2	Choline chloride : oxalic acid	34	−0.97
DES3	Choline chloride : malonic acid	10	−0.16
DES4	Choline chloride : citric acid	69	0.15
DES5	Choline chloride : phenylpropionic acid	20	1.12

Fig. 2 (a) Batch EL synthesis in the MWVIS-BR; (b) continuous EL synthesis process in the MWVIS-CSSR.

Table 2 Independent process factors and their levels for L9-TOD

Factors	Name	Units	−1 level	0 level	1 level
Ω_T	Reaction temperature	°C	80	90	100
Ω_S	Stirring speed	rpm	400	500	600
$\Omega_{NZF/PSCB}$	NZF to PSCB ratio	(wt%)	2	4	6
Ω_t	Synthesis time	min	30	45	60

Table 3 L9-TOD for one pot EL synthesis from PSCB

Ω_T (°C)	Ω_t (min)	$\Omega_{NZF/PSCB}$ (wt%)	Ω_S (rpm)	Ω_{EL} (mol%)	SD	SN ratio
80	30	2	400	20.50	±0.50	26.23
80	45	4	500	29.50	±0.15	29.39
80	60	6	600	27.50	±0.05	28.78
90	30	4	600	31.75	±0.50	30.03
90	45	6	400	44.10	±0.30	32.88
90	60	2	500	36.40	±0.10	31.22
100	30	6	500	47.10	±0.20	33.46
100	45	2	600	39.75	±0.30	31.98
100	60	4	400	50.20	±0.25	34.01

along with ethanol. The slurry diaphragm pump flow rates were controlled using the VFD controller and to monitor the reactor's temperature, three temperature probes were installed at various radial positions of the reactor. The reaction mixture was agitated with a turbine type mechanical impeller (Fig. 2(b)) at 500 rpm and the product was collected under steady state conditions after carefully monitoring the MW and VIS energy system at a controlled reactor temperature (100 °C). The reactor outlet was connected to a magnetic separator, where the NZF photocatalyst was separated. Subsequently, the residual slurry was connected to a three-fold vacuum separator unit to separate the humin. Finally, the unreacted ethanol and ethyl formate (EF) were separated through a vacuum evaporator and the product EL and DES were isolated through solvent extraction

and purification. Lastly, the recovered ethanol and DES were reintroduced into the reactor.

2.2.5. Plausible reaction mechanism and kinetic model formation. The plausible reaction pathways for the synthesis of EL from PSCB under optimal reaction conditions are shown in Scheme 1. The PSCB to EL conversion reaction initiated with the hydrolysis step where PSCB depolymerized to release hexose (glucose and mannose monomers) and pentose (mainly the xylose monomer) with the aid of hydrogen bond donor–acceptor complexes of the acidic DES and Lewis acidic sites of the NZF photocatalyst. Afterwards, 5EMF was formed from hexose and pentose (not shown in Scheme 1), which may follow two possible routes. In route-1, glucose and mannose were first alcoholised, yielding EDGP, which was then dehydrated to generate 5EMF. In route-2, glucose and mannose were first isomerized to produce fructose, followed by dehydration to produce 5HMF and subsequently, the 5HMF was alcoholised to yield 5EMF. Finally, the produced 5EMF further alcoholised and produced EL and ethyl formate (EF) along with ethanol.

During an experimental kinetic study of the continuous EL synthesis process, EDGP, 5EMF, EL, and EF were identified as the main generated products (Fig. 9). Additionally, glucose and 5HMF were detected in trace amounts in the product mix. Based on the above results, it was assumed that formation of EDGP from glucose or mannose takes place rapidly and the overall

Scheme 1 Possible reaction pathway for EL synthesis from PSCB (green colour represents route-1 and red colour represents route-2).

$$PSCB \longrightarrow EDGP \longrightarrow 5EMF \longrightarrow EL + EF$$
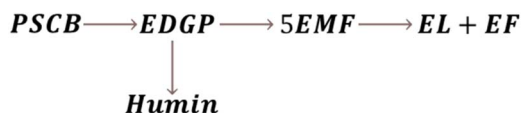$$\downarrow$$
$$Humin$$

Fig. 3   Simplified reaction scheme of EL synthesis from PSCB.

reaction pathway primarily follows route-1.[35] Moreover, formation of humin was also observed under optimized process conditions. Thus, the continuous PSCB to EL conversion process employing NZF and DES2 was simplified as Fig. 3.

Notably, during experimental investigation, it was observed that under non-catalytic conditions (without NZF and DES), PSCB underwent partial conversion to EDGP in the MWVIS-CSSR. Furthermore, in the presence of both the homogeneous acidic DES and heterogeneous NZF photocatalyst, PSCB was observed to convert to EL through parallel pathways, including both homogeneous and heterogeneous processes. Consequently, the overall rate of PSCB conversion ($-r_{PSCB}$) was formulated by combining the non-catalytic ($-r_{NC}$), homogeneous catalytic ($-r_{H1}$) and heterogeneous catalytic ($-r_{Ht1}$) conversion rate of PSCB. Notably, in formulating the rates for non-catalytic and homogeneous catalytic conversion, a pseudo-homogeneous irreversible first-order kinetic model was assumed, while for heterogeneous catalytic conversion of PSCB, the Eley–Rideal heterogeneous kinetic model was applied. In formulating the Eley–Rideal heterogeneous kinetic model, it was assumed that only ethanol was adsorbed on the NZF photocatalyst's surface, as PSCB's larger size (size range: −240 to +300 mesh; average size: 58 μm) prevented it from entering the pores of NZF (average surface pore size of the NZF: 48 nm, from Brunauer–Emmett–Teller (BET) analysis) and the surface reaction was the rate controlling step.

$$-r_{PSCB} = -[r_{NC} + r_{H1} + \rho_{NZF}r_{Ht1}] \tag{3}$$

Or,

$$-r_{PSCB} = k_{NC}C_{PSCB} + k_{H1}C_{PSCB} + \rho_{NZF}\frac{k_{Ht1}C_E}{1 + K_{A1}C_E + K_{D1}C_{EDGP}} \tag{4}$$

Accordingly, the formation rates of EDGP (eqn (5)), 5EMF (eqn (6)), EL (eqn (7)) and humin (eqn (8)) were also formulated by considering a homogeneous pseudo first order kinetic model and heterogeneous Eley–Rideal kinetic model. Notably, the product yields were calculated based on the holocellulose present in the PSCB.

$$r_{EDGP} = k_{NC}C_{PSCB} + k_{H1}C_{PSCB} - k_{H2}C_{EDGP} - k_{H3}C_{EDGP}$$
$$+ \rho_{NZF}\left[\frac{k_{Ht1}C_E}{1 + K_{A1}C_E + K_{D1}C_{EDGP}}\right.$$
$$\left. - \frac{k_{Ht2}C_{EDGP}}{1 + K_{A2}C_{EDGP} + K_{D2}C_{5EMF}}\right] \tag{5}$$

$$r_{5EMF} = k_{H2}C_{EDGP} - k_{H4}C_{5EMF}$$
$$+ \rho_{NZF}\left[\frac{k_{Ht2}C_{EDGP}}{1 + K_{A2}C_{EDGP} + K_{D2}C_{5EMF}} - \frac{k_{Ht3}C_{5EMF}}{1 + K_{A3}C_{5EMF} + K_{D3}C_{EL}}\right] \tag{6}$$

$$r_{EL} = k_{H4}C_{5EMF} + \rho_{NZF}\frac{k_{Ht3}C_{5EMF}}{1 + K_{A3}C_{5EMF} + K_{D3}C_{EL}} \tag{7}$$

$$r_{Humin} = k_{H3}C_{EDGP} \tag{8}$$

Here C_{PSCB} represents the concentration (mol L^{-1}) of holocellulose in PSCB, whereas C_E, C_{EDGP}, C_{5EMF}, C_{EF}, C_{Humin} and C_{EL} denote the concentration of ethanol, EDGP, 5EMF, EF, humin and EL, respectively. The NZF photocatalyst bulk density was denoted by ρ_{NZF} (g L^{-1}). The non-catalytic rate constant (min^{-1}) was represented by k_{NC} whereas the homogeneous catalytic rate constants (min^{-1}) for PSCB, EDGP, and 5EMF conversion processes were denoted by k_{H1}, k_{H2}, and k_{H4}. The heterogeneous catalytic rate constants (g of NZF per min) for PSCB, EDGP and 5EMF conversion processes were denoted by k_{Ht1}, k_{Ht2}, and k_{Ht3}. The adsorption equilibrium constants are represented by K_{A1}, K_{A2}, and K_{A3} and the desorption equilibrium constants are denoted by K_{D1}, K_{D2}, and K_{D3} respectively.

Finally, the observed rate of conversion or formation of each species was determined employing the CSSR design equation (eqn (9)) and the kinetic parameters of the formulated kinetic model equations (eqn (4)–(8)) at different temperatures were evaluated.

$$r_i = \frac{\vartheta_{Slurry}(C_i - C_{i0})}{V_{CSSR}} \tag{9}$$

Here, V_{CSSR} denotes the volume of the CSSR and ϑ_{Slurry} represents the volumetric slurry flowrate. C_i and C_{i0} represent the final and initial concentrations of the ith species, respectively. The activation energies of different reaction steps were calculated according to the Arrhenius equation.

$$k_i = A_{oi}e^{\left(-\frac{E_i}{RT}\right)} \tag{10}$$

Here T represents the reaction temperatures while E_i (kJ mol^{-1}) and A_{oi} are the activation energy and pre-exponential factor respectively. R is the universal gas constant (8.31 × 10^{-3} kJ mol^{-1} K^{-1}). The kinetic parameters were estimated by fitting experimental kinetic data using the fminsearch algorithm in the MATLAB R2014a software.

2.2.6. EL–biodiesel–diesel blending and engine performance of blended fuels. The continuously generated EL was isolated, purified, and then blended with B10 (90 vol% diesel and 10 vol% biodiesel) and B20 (80 vol% diesel and 20 vol% biodiesel) at concentrations of 5% and 10%. Afterwards, the characteristics of the synthesized EL and the resulting blended fuels (EL5B10, EL10B10, EL5B20, EL10B20) were examined (Table S2†). From Table S2,† it was observed that the EL blended fuels (EL5B10, EL10B10, EL5B20, EL10B20) showed enhanced characteristics, with a 3–6 °C higher flash point and a 1–3 °C

Table 4 Price of the individual feed, utility, product and byproduct streams

Stream	Stream type	Price (US$ per kg)	References
SCB	Feed stream	0.024	33
Ethanol	Feed stream	0.903	34
NaOH	Feed stream	0.212 065	
Peroxy-acetic acid	Feed stream	0.344 505	
ChCl	Feed stream	0.77	
Oxalic acid	Feed stream	0.56	
Electricity	Utility stream	0.19 (US$ per kWh)	34
Cooling water	Utility stream	0.001 318	34
Medium pressure steam	Utility stream	0.008 627	34
EL	Product stream	3	34
EF	Byproduct stream	2.16	
Lignin	Byproduct stream	0.5	38
Sodium acetate	Byproduct stream	0.545	39
Humin	Waste stream	−0.04	40

lower cloud point compared to B10 and B20. After property measurement, a four-stroke diesel engine (553 cc cylinder and 3.7 kW power output) was employed to assess the performance of the blended fuels and the exhaust emissions at engine speed ranging from 1000 to 1500 rpm were examined using an exhaust gas analyser with measurement capabilities for CO (0–15%), HC (0–20 000 ppm), CO_2 (0–20%), and NO_x (0–5000 ppm).

2.2.7. EL synthesis process sustainability analysis. To assess the overall sustainability of the EL synthesis process from sugarcane bagasse (SCB) under MWVIS, both techno-economic and environmental impact analyses were conducted and compared with individual irradiation systems. Cañon *et al.*[34] recently investigated the techno-economic analysis of EL production from Colombian rice straw at a processing capacity of 2000 kg h^{-1}. Thus, for techno-economic analysis of the SCB to EL conversion process, as outlined in the current study, processing capacity was upscaled to 2000 kg h^{-1} and simulated in Aspen Plus software. Following the techno-economic assessment, the environmental impacts associated with the upscaled process were examined using OpenLCA software.

2.2.7.1. Process scale-up and economic analysis. For techno-economic analysis, the SCB to EL conversion process was subdivided into four sections and modelled as four hierarchy blocks, *viz.* SCB PRETREATMENT, DES PREPARATION, EL PRODUCTION and PRODUCT PURIFICATION, using Aspen Plus software. During simulation of the SCB PRETREATMENT hierarchy block, the SCB, containing 10% moisture, was modelled as cellulose, hemicellulose and lignin content according to Table S1.† Additionally, information of the missing properties such as solid molar volume, solid heat capacity of cellulose, humin (insoluble solid) and lignin was collected from the ASPEN PLUS INHSPCD (NREL Biofuels) databank.[36] Notably, the screw feeder setup utilised in the current study was modelled as a pneumatic feeder during Aspen Plus simulation, where air was used to convey the solid PSCB–NZF mixture (Fig. S5†). In the simulation of the EL PRODUCTION hierarchy block, the MWVIS-CSSR was modelled as a custom CSTR with the help of ASPEN CUSTOM MODELER, where the estimated kinetic parameters of the EL synthesis process were used to simulate the PSCB to EL conversion process.

A Non-Random Two-Liquid with Redlich-Kwon (NRTL-RK) model was considered as the primary thermodynamic package for phase equilibrium and thermodynamic calculations. However, in order to successfully simulate the PRODUCT PURIFICATION block in Aspen Plus, we chose to utilize the COSMO-SAC property model for estimating activity coefficients, due to the absence of binary interaction parameters for DES2 with other components in the simulation. The COSMO data (sigma (σ) profile) for individual components (Fig. S2†) were determined through density functional theory (DFT) calculations carried out in the DMOL3 module of the Material Studio software.[37]

After successfully simulating the EL conversion process, economic analysis of the plant was conducted using the Aspen Plus Economic Analyzer, considering a 20 year plant life and a one-year construction period. Table 4 displays the prices of the individual feed stream, utility stream, waste stream, product, and byproduct stream. The price of NaOH (https://www.echemi.com/), peroxy-acetic acid (https://www.echemi.com/), oxalic acid (https://www.chemanalyst.com/ HYPERLINK "http://www.chemanalyst.com" \o "http://www.chemanalyst.com"www.chemanalyst.com), and EF (https://www.indiamart.com/) was obtained from various sources. Notably, the equipment cost of the MWVIS-CSSR was determined by combining the cost of a closed agitated tank with a similar capacity and the additional cost for MW and VIS generator units. The average reported cost of 100 kW microwave generators typically varies between 75 000 and 100 000 US$ depending on various design parameters.[41] Therefore, in the MWVIS-CSSR equipment cost calculation, a cost of 1000 US$ per kW for a 915 MHz MW generator was considered. Similarly, the equipment cost calculation for the MWVIS-CSSR included a pricing of 1000 US$ per kW for the VIS source.[42]

2.2.7.2. Environmental impact assessment. After economic analysis, the environmental impacts associated with the EL
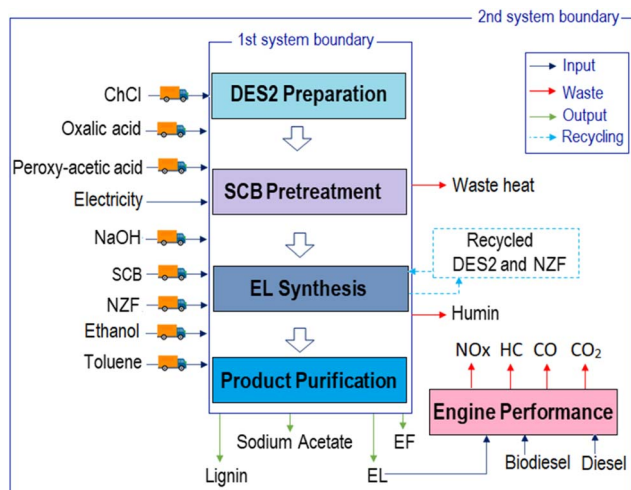
Fig. 4 System boundary for LCA analysis of the SCB to EL conversion process and EL blended fuels.

Fig. 5 (a) EL yield in the prepared DES (reaction conditions: $\varOmega_T$: 100 °C; $\varOmega_{NZF/PSCB}$: 4 wt%; $\varOmega_t$: 45 min; $\varOmega_S$: 500 rpm). (b) TGA analyses of the DES; (c) density and (d) viscosity of the DES.

synthesis process were analysed using OpenLCA 1.9 software. Additionally, the environmental impacts related to specific irradiation systems were scrutinized to comprehend the influence of energy consumption in both MW and VIS irradiation systems on the overall environmental footprint. To explore these impacts, a gate-to-gate life cycle assessment (LCA) approach was utilized, where the system boundary (Fig. 4; 1st system boundary) encompasses the transport of raw materials, the pretreatment of waste SCB, the preparation of a DES, and the synthesis and purification process of EL. In the context of transportation, it was assumed that the transportation of all raw materials would cover a distance of 100 kilometres using a 16 metric ton truck equipped with a EURO VI engine. Additionally, the waste humin generated in the EL synthesis process was considered to be managed through hazardous waste treatment, specifically underground deposition. It is noteworthy that all electric energy employed in the operation was considered to dissipate into the atmosphere as waste heat.[43] Moreover, to identify the optimum EL blending ratio in B10 and B20, environmental impact analysis for each blend was also performed employing the engine exhaust emission data though the gate to grave approach (Fig. 4; 2nd system boundary).

The life cycle inventory (LCI) database was prepared based on the Aspen Plus simulated data of the upscaled EL synthesis process. "ReCiPe Midpoint (H)" life cycle analysis methodology[44] with Ecoinvent database 3.5 was used to assess and evaluate the potential environmental impact indicators associated with the EL synthesis process. During LCA analysis, physical allocation was considered for the multioutput processes and LCA results were normalized based on "World ReCiPe H" normalization and a weighting factor.

3 Results and discussion

3.1. Screening of DESs in the MWVIS-BR

In Fig. 5(a), it is evident that the oxalic acid-based DES (DES2) exhibited the highest EL yield from PSCB in the presence of the
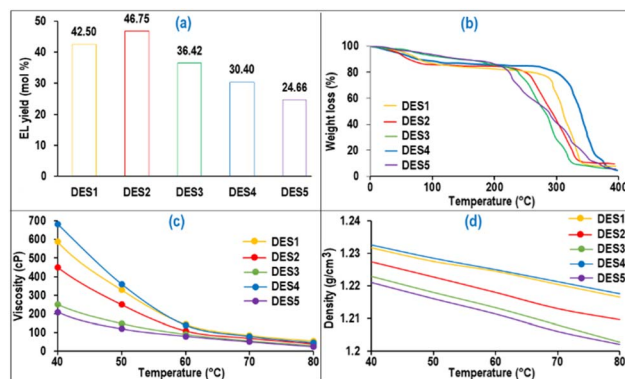
NZF photo-catalyst, despite its higher pH value compared to DES1. Interestingly, in the absence of the NZF photo-catalyst, DES1, with the lowest pH value, achieved the highest EL yield (31.0 mol%) compared to the other prepared DESs under the same reaction conditions. This discrepancy was attributed to the partial solubility of the NZF catalyst in DES1 at 100 °C, leading to its ineffective performance under VIS irradiation. Notably, the NZF photocatalyst was completely insoluble in DES2 and retained its magnetic properties, allowing easy separation from the reaction mixture and reuse for up to eight cycles without compromising EL yield. Additionally, TGA analysis (Fig. 5(b)) revealed that DES2 was thermally stable at the reaction temperature and it also has low viscosity (Fig. 5(c)) and density (Fig. 5(d)) at the reaction temperature, which facilitates the reaction. Thus, considering the experimental findings and the physical properties of the DESs (characterization details of DESs are given in ESI Section S3†), it could be concluded that DES2 is the most efficient medium for synthesizing EL from PSCB in the presence of the NZF photo-catalyst. As a result, for subsequent investigations, the EL synthesis process was conducted using DES2 as the chosen medium.

3.2. Optimization of the EL synthesis process in the MWVIS-BR

Analysis of variance (ANOVA) for the EL synthesis process in the MWVIS-BR indicated that the $\varOmega_T$ and $\varOmega_{NZF/PSCB}$ were the most statistically significant factors (p-value < 0.05) (Table 5). The normal probability plot of residuals and the model fit summary

Table 5 Analysis of variance (ANOVA)

Source	DF	Adj. SS	Adj. MS	F-value	P-value
Regression	4	749.93	187.484	28.10	0.003
$\varOmega_T$	1	591.03	591.034	88.58	0.001
$\varOmega_t$	1	36.26	36.260	5.43	0.080
$\varOmega_{NZF/PSCB}$	1	81.03	81.034	12.14	0.025
$\varOmega_S$	1	41.61	41.607	6.24	0.067
Error	4	26.69	6.672		
Total	8	776.62			

Table 6 S/N ratio of the EL synthesis process

Level	Ω_T	Ω_t	$\Omega_{NZF/PSCB}$	Ω_S
1	28.14	29.91	29.81	31.05
2	31.38	31.42*	31.15	31.36*
3	33.15*	31.34	31.71*	30.27
Delta	5.01	1.51	1.90	1.09
Rank	1	3	2	4

along with correlation between process factors and Ω_{EL} is shown in Fig. S3.† Notably, Table 6 reveals that the process factors with higher Δ values showed a stronger influence on the response factor (Ω_{EL}). Accordingly, the order in which the relative significance of the process factors on the response (Ω_{EL}) could be arranged is: $\Omega_T > \Omega_{NZF/PSCB} > \Omega_t > \Omega_S$. Moreover, the highest S/N ratio value for each process factor is denoted by an asterisk (Table 6), which showed that the optimized process factors were 100 °C (Ω_T), 6 wt% ($\Omega_{NZF/PSCB}$), 45 min (Ω_t), and 500 rpm (Ω_S), which provided a maximum experimental 54.50 mol% EL yield (selectivity: 97.85%) in the MWVIS-BR in the presence of DES2 medium.

3.3. Individual parametric effects on the EL synthesis process in the MWVIS-BR

After optimization, the individual impact of process factors on the EL synthesis process under optimized conditions was investigated. The analysis of the effect of reaction temperature on EL yield, as depicted in Fig. 6(a), indicated that beyond a reaction temperature of 100 °C, the EL yield began to decrease, possibly due to the formation of humin from EDGP at higher temperatures. Furthermore, the EL yield monotonically increased with increasing stirring speed up to 500 rpm (Fig. 6(b)) where mass transfer resistance was negligible which was confirmed through external and internal mass transfer calculations employing the Mears criterion and Weisz–Prater

criterion respectively.[45] However, the EL yield started to decrease due to the vortex formation when the stirring speed was extended beyond the optimal level. The effect of batch reaction time on EL yield is shown in Fig. S4.†

The impact of the NZF to PSCB ratio ($\Omega_{NZF/PSCB}$) on EL yield, depicted in Fig. 6(c), revealed that there was a marginal increase in EL yield beyond the optimal $\Omega_{NZF/PSCB}$ value of 6 wt%. A similar trend was also observed when the DES2 to PSCB ratio was increased beyond 5 wt/wt. On the other hand, the optimum ethanol loading per gram of PSCB was found to be 10 ml; beyond that point, the EL yield started to decrease (as depicted in Fig. 6(d)). This decrease in yield can be attributed to the higher ethanol loading, which results in a reduction of acid concentration within the reaction medium and a decrease in the absorption capacity of MW.

3.4. MWVIS-CSSR performance study in the EL synthesis process

The performance of the 5 L MWVIS-CSSR was examined in the EL synthesis process at various feed flow rates while maintaining the otherwise optimized batch process conditions, viz. 100 °C (Ω_T), 6 wt% ($\Omega_{NZF/PSCB}$), and 500 rpm (Ω_S). Fig. 7(a) shows that under steady state conditions, a similar EL yield to that in the MWVIS-BR (54.50 mol%) could be achieved in the MWVIS-CSSR at a slurry feed flowrate of 35 ml min^{-1} (space time: 142 min). Notably, further decreasing the feed flow rate didn't increase the EL yield much (2.7% EL yield increment). The reusability study of the DES2 medium was conducted using a fresh NZF photocatalyst in the MWVIS-CSSR which revealed that the oxalic acid–choline chloride-based DES medium could be easily reused up to 5 times without compromising the EL yield (Fig. 7(b)). Importantly, no decrease in the efficacy of the NZF photocatalyst up to eight cycles, as measured by EL yield, was observed throughout the NZF reusability study.

Interestingly, to facilitate comparison, experimental runs for EL production from SCB and cellulose were conducted at a feed flow rate of 35 ml min^{-1}. Notably, EL yield from cellulose was 43 mol%, while EL from SCB reached 58.60 mol%. However, despite the higher EL yield from SCB compared to PSCB, separating EL and recycling the DES2 from the product mixture after the reaction proved to be challenging.

The impact of individual and combined MW and VIS energy systems on EL yield in the large MWVIS-CSSR was also explored and illustrated in Fig. 8(a). This inquiry revealed a synergistic
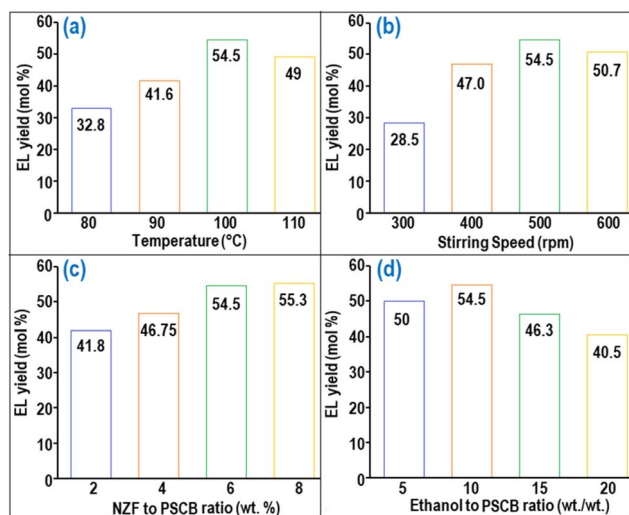

Fig. 6 Effect of (a) temperature and (b) stirring speed on EL yield, (c) NZF to PSCB ratio and (d) ethanol to PSCB ratio on EL yield in the MWVIS-BR.
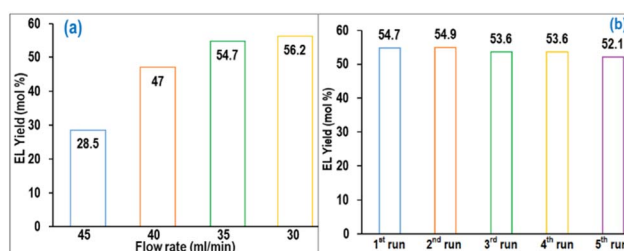

Fig. 7 (a) Effect of feed flow rate on EL yield. (b) DES2 reusability study in the MWVIS-CSSR.
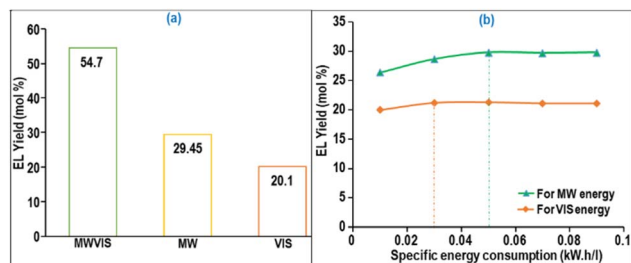
Fig. 8 (a) EL production and (b) specific energy consumption by the MW and VIS system in a 5 L MWVIS-CSSR.

effect in the combined MW and VIS irradiation system, significantly enhancing EL yield (54.7 mol%) compared to individual MW (29.45 mol%) and VIS (20.1 mol%) irradiation systems. The synergistic effect of MW-induced heating, driven by dipolar rotation and the ionic conduction mechanism in the presence of DES2,[46] coupled with the absorption of VIS energy by the NZF photocatalyst, modifies the internal energy of the reacting molecules and decreases the activation energy,[47] enabling higher EL yield in the presence of the MWVIS system.

Notably, the specific energy consumption for achieving 54.7 mol% EL yield with combined MW (0.05 kW h L^{-1}) and VIS (0.02 kW h L^{-1}) energy (Fig. 8(b)) in the large 5 L CSSR (total specific energy consumption: 0.07 kW h L^{-1}) was substantially lower than in the smaller 15 ml batch reactor system (6 kW h L^{-1}). This observation is in line with Bermúdez et al.'s[27] findings, showing that raising the sample weight from 5 to 100 g leads to a significant 90–95% reduction in the MW specific energy consumption for sample heating, while beyond 200 g, the specific energy consumption of MW energy remains relatively constant.

3.5. Kinetics parameters evaluation for the EL synthesis process in the MWVIS-CSSR

The PSCB to EL continuous conversion kinetic data (Fig. 9) obtained from the MWVIS-CSSR at different reaction temperatures under otherwise optimal reaction conditions were fitted in the formulated kinetic models employing MATLAB R2014a. Notably, the formulated kinetic models exhibit remarkable agreement with experimental data, showcasing high R^2 adj. ($\geq$0.95) and low RMSE values ($\leq$5.15 × 10^{-7}) (Table 7). Accordingly, the kinetic rate constants for different reaction steps involved in the PSCB to EL synthesis process were evaluated and tabulated in Table 7. Analysis of Table 7 revealed that the rate of the conversion reaction from PSCB to EDGP was significantly slower in the heterogeneous catalytic route (2.0 × 10^{-4} g of NZF per min) compared to the homogeneous counterpart (0.0428 min^{-1}). However, the heterogeneous catalyst, NZF, demonstrated significant advancements in enhancing the rate of the EDGP to 5EMF and 5EMF to EL conversion steps (Table 7), aligning closely with the performance of the homogeneous counterpart, i.e. DES2. Besides, the evaluated activation energies (E) and pre-exponential factors (A_o) (Table 8) suggested that the conversion reaction from EDGP to humin exhibits the highest activation energy (96.467 kJ mol^{-1}) among all the reaction steps involved in the PSCB to EL synthesis process, suggesting the NZF photocatalyst and DES2 could effectively inhibit humin generation.

3.6. Techno-economic analysis of the SCB to EL conversion process

Fig. 10 depicted a successful simulation of the SCB to EL conversion process, showcasing four hierarchical blocks (DES PREPARATION, SCB PRETREATMENT, EL PRODUCTION, and
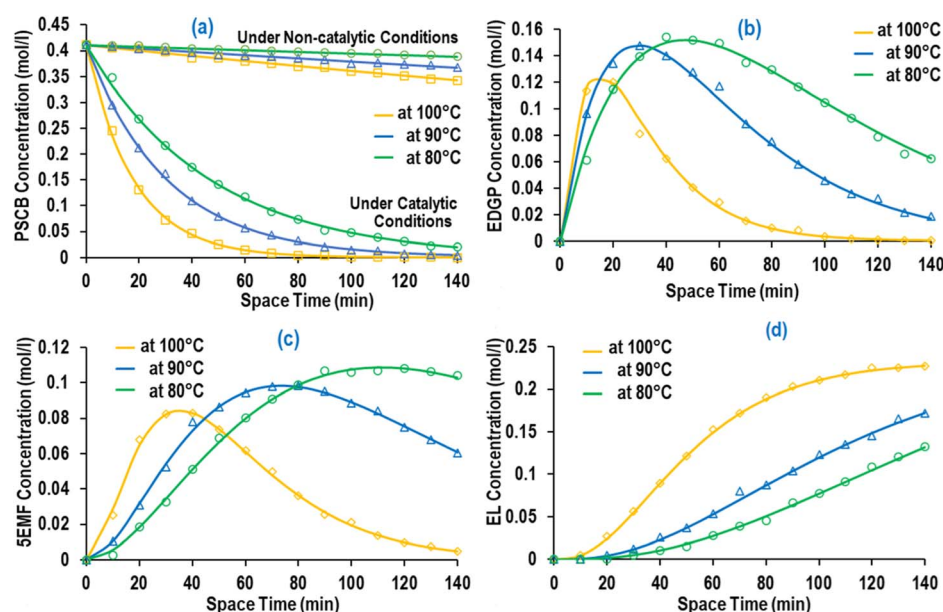

Fig. 9 (a) PSCB (under catalytic and non-catalytic conditions), (b) EDGP, (c) 5EMF and (d) EL concentrations at different reaction temperatures [line: predicted yield; marker: actual yield].

Table 7 Estimated kinetic parameters of PSCB to EL conversion reaction steps

Temperature (K)	Rate constants								R^2	R_{adj}^2	RMSE
	k_{NC}	k_{H1}	k_{H2}	k_{H3}	k_{H4}	k_{Ht1}	k_{Ht2}	k_{Ht3}			
373	0.0013	0.0428	0.0128	0.0152	0.035	2.0×10^{-4}	0.0037	0.0028	0.96	0.95	5.15×10^{-7}
363	0.0008	0.0306	0.0116	0.0122	0.014	1.0×10^{-4}	0.0025	0.0023	0.99	0.99	5.77×10^{-7}
353	0.0004	0.0205	0.0075	0.007	0.006	4.44×10^{-5}	0.0020	0.0017	0.98	0.97	5.64×10^{-7}

Table 8 Estimated activation energy and pre-exponential factors of PSCB to EL conversion reaction steps

Reaction step	Non-catalytic reaction pathway		Homogeneous catalytic reaction pathway		Heterogeneous catalytic reaction pathway	
	E (kJ mol^{-1})	A_o	E (kJ mol^{-1})	A_o	E (kJ mol^{-1})	A_o
PSCB to EDGP conversion	64.601	1.49×10^6	40.167	18 196.78	91.520	1.53×10^9
EDGP to 5EMF conversion			29.161	160.20	33.185	161.41
5EMF to EL conversion			42.440	14 071.40	26.590	15.26
EDGP to humin conversion			96.467	1.11×10^{12}		

PRODUCT PURIFICATION) along with corresponding feed and product flow rates. The SCB PRETREATMENT hierarchical block was simulated with a processing capacity of 2000 kg h^{-1} of SCB, resulting in the production of 378 kg h^{-1} of lignin, 4314 kg h^{-1} of sodium acetate, and 1423 kg h^{-1} of PSCB. Notably, the RSTOIC model was used to simulate the pretreatment and neutralization reactor. A detailed process flow-diagram of the simulated SCB PRETREATMENT is shown in Fig. S6.†

Within the EL PRODUCTION hierarchy block (Fig. 11), the MWVIS-CSSR was simulated as a single CSTR (reactor volume: 72 m^3, space time: 142 min), enabling the processing of 30 812 kg h^{-1} of the reaction mixture. Following the completion of the reaction, the NZF magnetic photocatalyst was separated using a magnetic separator. Subsequently, humin was isolated through filtration, and the remaining liquid product mixture was directed to the PRODUCT PURIFICATION hierarchy block. Notably, during the humin separation process, it was assumed that 1% of the total utilized DES2 was lost.

Although the MWVIS-CSSR was simulated as a single reactor (72 m^3 volume), upscaling to such large volume poses challenges. One of the key challenges associated with large MW or photo-reactors is uneven distribution of electromagnetic energy due to their short penetration depth in the reactor medium. In this context, a well-executed reactor design typically involved the consideration of the penetration depth of MW within the reaction medium, in conjunction with other conventional design factors. Goyal et al.[48] reported the significance of considering the microwave penetration depth when the reactor's maximum diameter exceeds four times that depth, in order to achieve consistent and uniform microwave heating. Based on complex permittivity [$\varepsilon(i\omega) = \varepsilon(\omega)' - i\varepsilon(\omega)''$] (Fig. 12(a)) and the calculated penetration depth from eqn (1) (0.246 m) of DES2–ethanol medium at 915 MHz MW frequency, it can be observed that the 5 liter MWVIS-CSSR can be easily scaled up to 1 m^3 volume (by increasing the reactor height and diameter by 6 times, while maintaining the same height-to-diameter ratio as

in the MWVIS-CSSR). Conversely, in terms of scaling up the CSSR with respect to VIS penetration depth poses no challenges, as the size of the Ni$_{0.5}$Zn$_{0.5}$Fe$_2$O$_4$ photocatalyst is smaller (<30 nm) than the VIS penetration depth (Fig. 12(b)) and the reaction medium exhibits transparency to VIS irradiation. Notably, various companies have already designed and implemented industrial-scale MW intensified CSSR (https://www.nanomagtech.com/) and photo-CSSR (https://www.ekato.com/) systems for different reaction applications; however, no previous company reported or designed a combined MW and VIS irradiated large-scale CSSR system. Thus, based on the MW and VIS energy penetration depths in our reaction medium and insights drawn from analogous large-scale industrial reactor designs, it would be practical to employ 72 CSSRs with a 1 m^3 reactor volume each, connected in parallel instead of using a single 72 m^3 single CSSR. This approach will not only guarantee consistent MW heating and VIS absorption by the reaction medium but also reduce the issue of uneven residence time distribution, which is a concern when using a large single CSSR.

Fig. 13 illustrates the simulated PRODUCT PURIFICATION hierarchical block, involving crucial unit operations such as distillation, extractions, and evaporation for the efficient separation of EL, DES2, ethanol, and EF. The hierarchical block commenced with distillation column 1, accomplishing complete separation of EF and a partial separation of ethanol from the product mixture. Subsequently, the remaining product mixture was sent to distillation column 2, where complete separation of ethanol was achieved. An extractor was then used to separate DES2 from the bottom product of distillate 2, employing toluene as the extracting solvent. Finally, EL (purity >99%) was separated from the extraction solvent by evaporating and recycling the toluene. Notably, in the purification process, DES2 served as an entrainer[49] in distillation column 3, facilitating the separation of ethanol from the EF–ethanol mixture that was initially obtained as a distillate from distillation
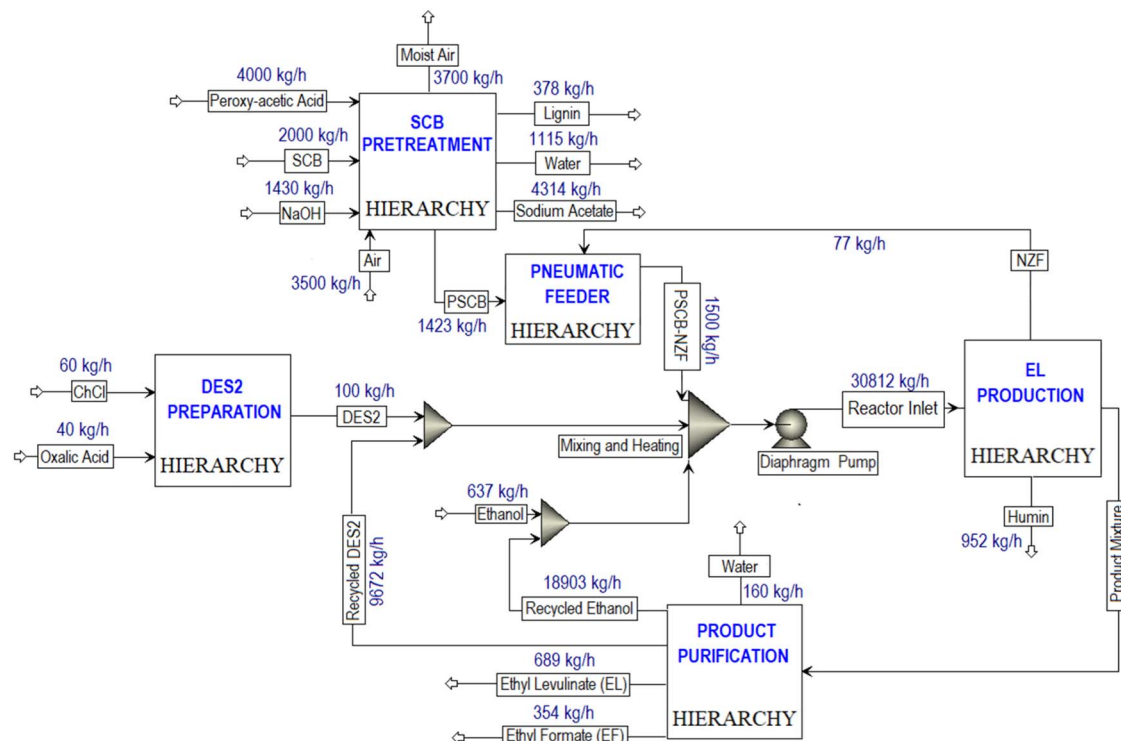
Fig. 10 Simulated process flow diagram of the SCB to EL conversion process.

column 1. Subsequently, EF was completely isolated from DES2 through evaporation, resulting in the collection of 99% pure EF, while DES2 was recycled back into distillation column 3.

In Fig. 14(a), the depicted data illustrated the overall capital expenses (CAPEX) and annual operating expenses (OPEX) associated with the simulated conversion process from SCB to EL, conducted at a processing capacity of 2000 SCB per hour. Analysis of Fig. 14(a) revealed that raw material costs constituted the predominant share of the total annual OPEX, comprising 45%, with utility costs following closely at 34%. On the other hand, Fig. 14(b) highlighted that the major equipment contributing to the total equipment costs includes the reactors (50%), followed by the distillation column (26%) and heat exchanger (16%). Notably, within the total reactor cost (cost of the pretreatment reactor, neutralizer and MWVIS-CSSR), the MWVIS-CSSR alone accounted for a total cost of 2.89×10^6 US\$, representing 67% of the total reactor cost. Despite the higher

cost of the MWVIS-CSSR, the annual electricity consumption cost of the MWVIS system represents only 11% of the total annual utility cost, amounting to a total of 4.92×10^5 US\$. The number of magnetrons used in a reactor significantly impacts its operational cost due to their low efficiency in converting electrical energy to microwave power.[50] Conversely, the power rating of the magnetrons influences the purchase cost of the reactor, as higher power ratings typically lead to lower purchase costs.[51] Therefore, it is important to optimize the employed magnetron system in order to enhance the energy savings. The cost of the MWVIS-CSSR can also be reduced by employing cutting-edge solid-state microwave generators which offers substantial cost benefits over traditional magnetrons by improving efficiency and reducing maintenance and operational expenses.[52]

Upon commencement of operations, the simulated process reveals an annual product sale of 3.96×10^7 US\$, with $1.74 \times$
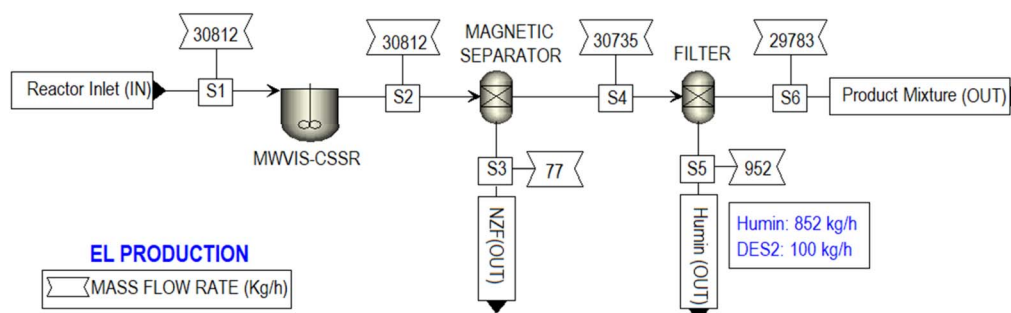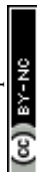

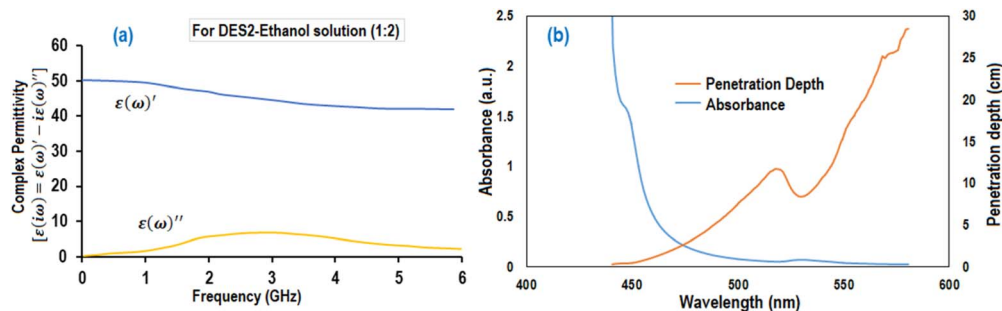**Fig. 11** Simulated process flow diagram of the EL PRODUCTION hierarchy block.

Fig. 12 (a) Complex permittivity of DES2. (b) UV-VIS absorption spectroscopic analysis of the NZF photocatalyst in DES2 medium.

10^7 US\$ from annual EL sales and an additional 6.42×10^6 US\$ stemming from annual EF sales. The sales revenue data provide insightful financial metrics for the simulated process, including a robust internal rate of return (IRR) of 54.25% with a net present value (NPV) of 8.22×10^5 US\$, signifying the project's profitability. Additionally, the payback period is estimated at 4.91 years (including a 1 year construction period), demonstrating the time required for the initial investment to be recouped through generated profits. Zhuo *et al.*[53] conducted an economic analysis on large scale EL production from corn straw, with an annual processing capacity of 70 000 tons of corn straw and reported that the calculated IRR of the large-scale production system was 35.08% and the payback period was 5.32 years. Notably, economic analyses were also carried out for the SCB to EL conversion process utilizing the MW-CSSR and VIS-CSSR, which revealed that the process involving the MW-assisted CSSR yielded an IRR of 24.5% with a payback period of 13.45 years whereas the process involving the VIS-assisted

CSSR showed no economic profit within the plant's lifetime of 20 years. Therefore, from the economic analysis, it is evident that the utilization of the MWVIS-CSSR significantly enhances the financial feasibility and attractiveness of the continuous SCB to EL conversion process.

3.7. Engine performance and exhaust analysis

The engine performance analysis data, involving brake thermal efficiency and brake-specific fuel consumption (BSFC) for various EL–biodiesel–diesel blended fuels (EL5B10, EL10B10, EL5B20, EL10B20) at 1500 rpm engine speed, is presented in Fig. 15(a and b). Notably, an increase in EL vol% in B10 enhanced the brake thermal efficiency (1–2%), while increasing EL vol% from 5% to 10% in B20 showed an adverse effect, leading to a decrease in the thermal efficiency (Fig. 15(a)). However, the BSFC was found to slightly increase (1–2.7%) with the augmented blending proportion of EL in both B10 and B20 (Fig. 15(b)). These observations emphasize that incorporating
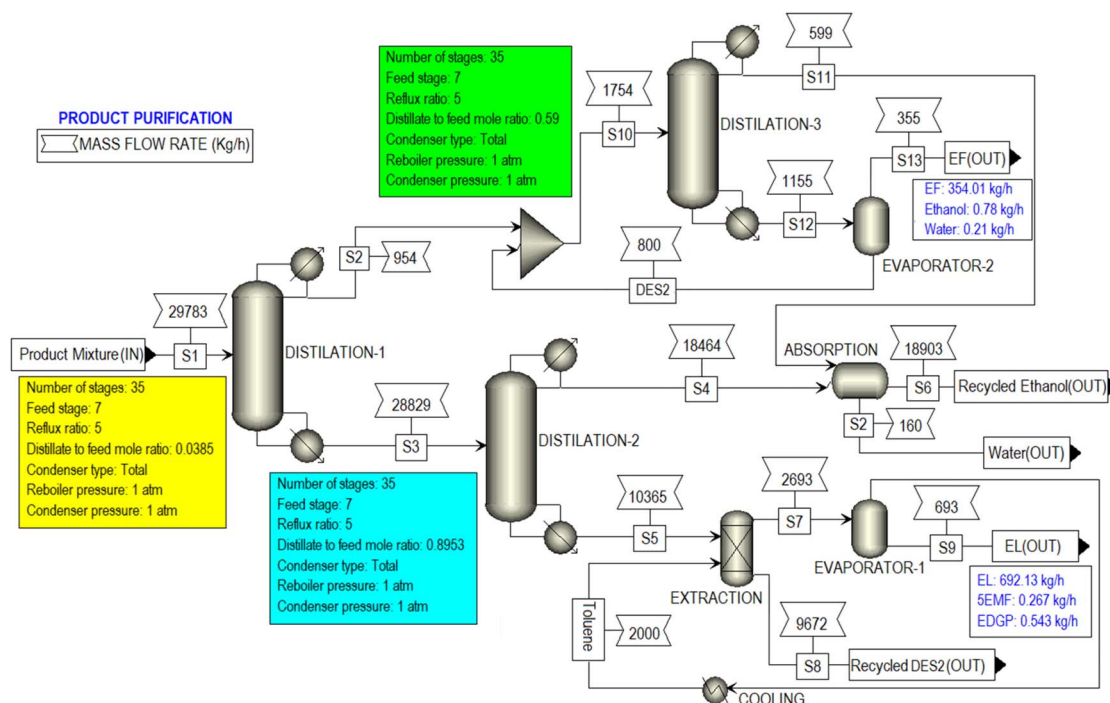

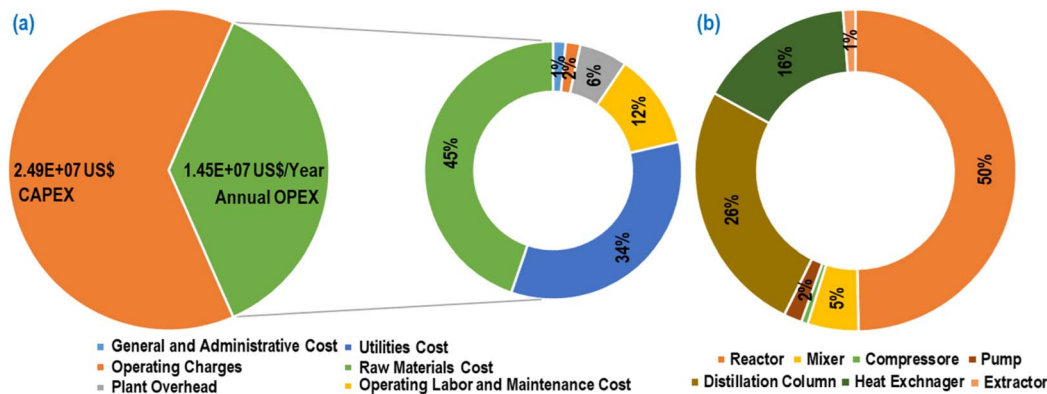**Fig. 13** Simulated process flow diagram of the PRODUCT PURIFICATION hierarchy block.

Fig. 14 (a) Total CAPEX and annual OPEX of the SCB to EL synthesis process. (b) Share of major equipment in the total equipment costs.

5 vol% EL in both B10 and B20 has the potential to enhance engine efficiency.

Fig. 15(c(i–iv)) illustrate the HC, NO$_x$, CO$_2$, and CO exhaust emissions for B10, B20, and EL-blended fuels (EL5B10, EL10B10, EL5B20, EL10B20). The HC emission data (Fig. 15(c(ii))) demonstrates a notable reduction with 5 vol% (HC reduction: 21–22%) and 10 vol% EL blending (HC reduction: 29–31%), compared to reference fuels B10 and B20. This reduction in HC emissions is ascribed to improved combustion in the combustion chamber, facilitated by the presence of oxygen (33 wt%) in EL.[54] Notably, the NO$_x$ emission (Fig. 15(c(ii))) values for EL-blended fuels were found to increase with increasing EL content; however they were less than those of B10 and B20. The rise in NO$_x$ emissions can be attributed to the increased combustion efficiency with higher EL content which leads to elevated maximum temperatures during the combustion of EL-blended fuels, creating conditions that favour the formation of NO$_x$.[55] Moreover, as the EL vol% in the EL-blended

fuels increased, CO emissions (Fig. 15(c(iii))) exhibited a gradual decrease (7.5–20% at 5 vol% EL blending; 17.5–40% at 10 vol% EL blending), while CO$_2$ emissions (Fig. 7(c(iv))) showed a gradual increase (4.5–8% at 5 vol% EL blending; 6–10% at 10 vol% EL blending) compared to the reference blends, B10 and B20, at a diesel engine speed of 1500 rpm.

3.8. Environmental sustainability analysis of the SCB to EL conversion process

Fig. 16(a) illustrates the normalized environmental impacts (per person per year) of the most significant ReCiPe midpoint (H) impact indicators associated with the simulated continuous EL synthesis process under MWVIS irradiation. The use of fossil fuels for transporting chemicals and waste SCB,[56] along with the utilization of coal-based electricity,[57] results in significant emissions of nitrates and nitrogen oxides (NO$_x$). These emissions contribute substantially to marine ecotoxicity (0.08142), freshwater ecotoxicity (0.05277), freshwater eutrophication
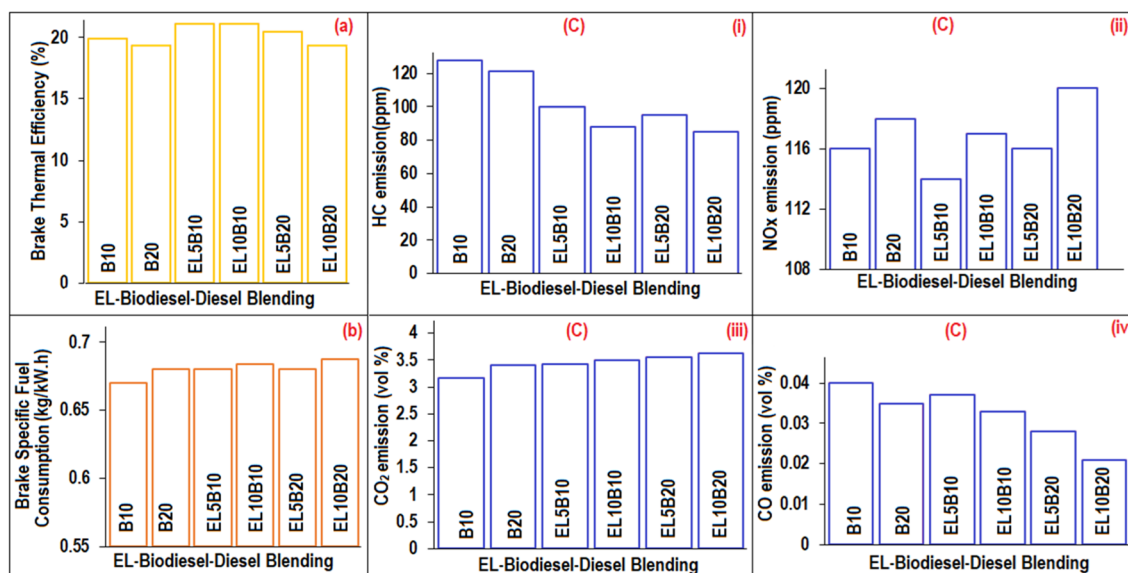

Fig. 15 (a) Brake thermal efficiency, (b) brake specific fuel consumption and (c) exhaust emission analyses: (i) HC, (ii) NO$_x$, (iii) CO$_2$, and (iv) CO of different blends.
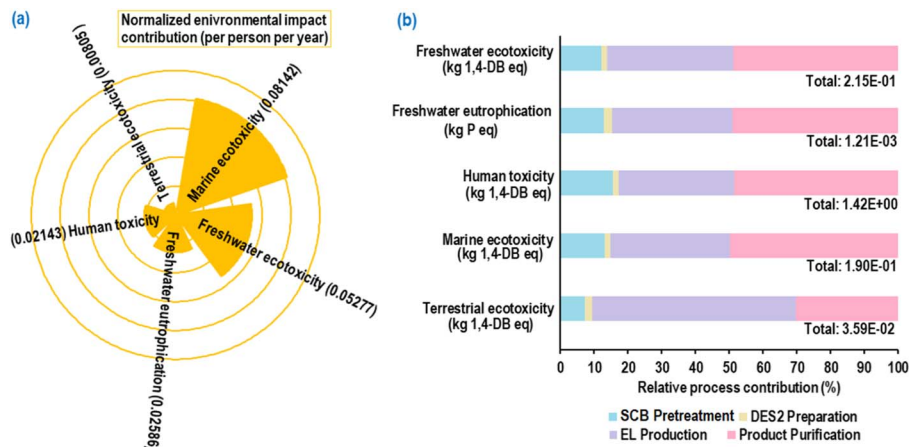
Fig. 16 (a) Normalized environmental impact contribution; (b) relative percentage contribution of sub-processes in most prominent environmental impact indicators associated with the simulated continuous EL conversion process under MWVIS.

(0.02586), human toxicity (0.02143) and terrestrial ecotoxicity (0.00805). Furthermore, the breakdown of percentage contributions by sub-processes in the significant indicators (Fig. 16(b)) revealed that product purification and EL production sub-processes were the primary contributors, followed by SCB pretreatment and DES2 preparation. The observed pattern is attributed to the utilization of coal-based steam and electricity to meet the high energy demand during product purification and EL production. Notably, Cañon *et al.*[34] conducted an LCA analysis of the ethyl levulinate production process from Colombian rice straw derived levulinic acid and reported a comparable freshwater eutrophication value (1.624×10^{-3} kg P eq.), slightly higher than the result obtained in the present study, indicating the environmental sustainability of the current process. The other minor environmental impact indicators are associated with the simulated EL conversion process and their normalized contributions are presented in ESI Fig. S7.†

A comparative environmental impact assessment study (Fig. 17(a)) for reactor systems indicated that the MWVIS-CSSR has less environmental impact in all indicators compared to MW-CSSR and VIS-CSSR systems. Thus, the synergistic MWVIS irradiation system not only enhanced the EL yield, but also had less environmental impacts on marine ecotoxicity, freshwater

ecotoxicity, freshwater eutrophication, human toxicity and terrestrial ecotoxicity by 40–60%, 41–62%, 40–60%, 39–61% and 9–17%, respectively in comparison with the MW and VIS systems.

Interestingly a comparative environmental impact analysis based on the blended fuel exhaust emission (Fig. 15(c)) and energy output data (Table S2†) showed that 5 vol% EL blending with B10 exhibited the least environmental impact in terms of climate change (kg CO_2 eq.) among all other fuel blends (Fig. 17(b)). Consequently, the integration of 5 vol% EL into B10 (biodiesel–diesel: 10 : 90 vol%) could significantly diminish overall environmental impacts, despite the B10EL5 blend showing elevated HC and CO emissions compared to other EL–biodiesel–diesel blends. A plausible explanation for this phenomenon could be the reduced NO_x emissions by B10EL5 compared to other blends, thereby establishing itself as a less significant contributor to climate change (1.72×10^{-2} kg CO_2 eq.).[58]

The comprehensive evaluation of both techno-economic and environmental impact analyses revealed that the continuous EL conversion process utilizing the integrated MWVIS irradiation system in a CSSR demonstrated enhanced overall process sustainability. This was evident in terms of both economic feasibility and environmental sustainability when compared to
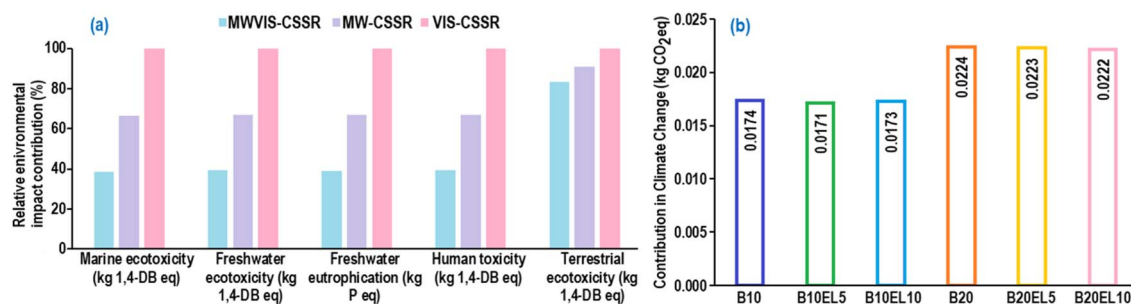

Fig. 17 (a) Relative environmental impact contribution of different reactor systems in the EL synthesis process [the maximum result of each indicator was set to 100%]; (b) global warming contribution of different EL blended fuels.

employing individual irradiation systems. The synergistic effect of MW and VIS irradiation in the presence of the NZF photocatalyst and DES2 medium contributed to improved efficiency and cost-effectiveness, and reduced environmental impacts, making it a promising approach for continuous ethyl levulinate production.

4 Conclusion

Sustainable continuous valorisation of pretreated sugarcane bagasse (PSCB) into ethyl levulinate (EL) was achieved employing an innovative microwave-visible irradiated continuous stirred slurry reactor (MWVIS-CSSR). Under mild reaction conditions (142 min residence time and 100 °C reaction temperature), the MWVIS-CSSR could render 54.7 mol% EL yield in the presence of a magnetic $Ni_{0.5}Zn_{0.5}Fe_2O_4$ (NZF) photocatalyst and oxalic acid–choline chloride based acidic deep eutectic solvent (DES2). Remarkably, the synergistic impacts of MW and VIS irradiation substantially augmented the EL yield (54.7 mol%), considerably exceeding the yields achieved with individual application of MW (29.45 mol%) and VIS (20.1 mol%) irradiation. Moreover, the developed novel reaction kinetic model for the PSCB to EL conversion process, formulated by considering parallel non-catalytic and homogeneous–heterogeneous catalytic routes, has been proven to accurately interpret the experimental data. The techno-economic study and comparative environmental impact assessment revealed that the continuous conversion of sugarcane bagasse to EL employing the MWVIS-CSSR exhibited superior economic feasibility (internal rate of return: 54.25%) and had less environmental impact (marine ecotoxicity: 1.90×10^{-1} kg 1,4-DB eq., freshwater ecotoxicity: 2.15×10^{-1} kg 1,4-DB eq. and human toxicity: 1.42 kg 1,4-DB eq.) compared to the EL conversion process in the individual MW-CSSR and and VIS-CSSR. Besides, environmental impact analysis based on the exhaust emission of EL–biodiesel–diesel blends showed that the 5 vol% EL blending in B10 exhibited the least environmental impact in terms of climate change (kg CO_2 eq.). Thus, the current continuous EL synthesis process, along with its subsequent application in assessing engine performance and the engine emission profile, not only underscores the potential for sustainable EL production through leveraging sugarcane bagasse but also signifies a significant step toward addressing energy efficiency and environmental concerns in the realm of drop-in-biofuel synthesis and its sustainable applications towards improvement in diesel engine performance and mitigation of adverse climate changes.

Data availability

Supporting data for the findings are available in the ESI† of this manuscript.

Author contributions

Sourav Barman: conceptualization, methodology, software, data collection & interpretation, validation. Rajat Chakraborty: conceptualization, visualization, supervision, funding acquisition, review, editing & overall guidance. All authors read and approved the final manuscript.

Conflicts of interest

There are no conflicts to declare.

Acknowledgements

References

1 A. A. Patil, R. R. Joshi, A. J. Dhavale and K. S. Balwan, *Int. J. Eng. Res. Technol.*, 2019, **6**, 1359–1361.
2 B. Tesfa, R. Mishra, C. Zhang, F. Gu and A. D. Ball, *Energy*, 2013, **51**, 101–115.
3 J. S. Lee, J. Y. Park, D. K. Kim, J. P. Lee, S. C. Park and Y. J. Kim, *Bioresour. Technol.*, 2008, **99**, 1196–1203.
4 B. C. Windom, T. M. Lovestead, M. Mascal, E. B. Nikitin and T. J. Bruno, *Energy Fuels*, 2011, **25**, 1878–1890.
5 D. Unlu, N. Boz, O. Ilgen and N. Hilmioglu, *Open Chem.*, 2018, **16**, 647–652.
6 V. Pace, P. Hoyos, L. Castoldi, P. Domínguez de María and A. R. Alcántara, *ChemSusChem*, 2012, **5**, 1369–1379.
7 Y. Kuwahara, H. Kango and H. Yamashita, *ACS Sustain. Chem. Eng.*, 2017, **5**, 1141–1152.
8 F. Ye, D. Zhang, T. Xue, Y. Wang and Y. Guan, *Green Chem.*, 2014, **16**, 3951–3957.
9 H. Liu, Y. Kong, W. Song, R. Zhang, J. Zhang, Y. Sun and L. Peng, *Chem. Eng. J.*, 2024, **481**, 148559.
10 Q. Guan, T. Lei, Z. Wang, H. Xu, L. Lin, G. Chen, X. Li and Z. Li, *Ind. Crops Prod.*, 2018, **113**, 150–156.
11 M. Sert, *Renew. Energy*, 2020, **153**, 1155–1162.
12 A. Hu, H. Wang and J. Ding, *ACS Omega*, 2022, 7, 33192–33198.
13 H. C. Nguyen, H. C. Ong, T. T. Pham, T. K. Dinh and C. H. Su, *Int. J. Energy Res.*, 2020, **44**, 1698–1708.
14 H. Liu, Y. Zhang, T. Hou, X. Chen, C. Gao, L. Han and W. Xiao, *Fuel Process. Technol.*, 2018, **174**, 53–60.
15 S. U. Raut, S. A. Deshmukh, S. H. Barange and P. R. Bhagat, *Catal. Today*, 2023, **408**, 81–91.
16 C. Castañeda, J. J. Martínez and A. Mesa, *Rev. Fac. Ing., Univ. Antioquia*, 2022, **105**, 29–36.
17 J. S. Jang, S. J. Hong, J. S. Lee, P. H. Borse, O. S. Jung, T. E. Hong, E. D. Jeong, M. S. Won, H. G. Kim and J. Korean, *Phys. Soc.*, 2009, **54**, 204–208.
18 S. Zhang, R. Shi and Y. Tan, *J. Solution Chem.*, 2018, **47**, 1112–1126.
19 O. K. Nimisha, M. Akshay, S. Mannya and A. R. Mary, *Mater. Today: Proc.*, 2022, **66**, 2370–2373.
20 R. Samanta and R. Chakraborty, *Renew. Energy*, 2023, **210**, 842–858.
21 S. Barman, S. Roy Choudhury and R. Chakraborty, *Environ. Sci. Pollut. Res.*, 2024, 1–14.

22 K. S. Konde, S. Nagarajan, V. Kumar, S. V. Patil and V. V. Ranade, *Sustainable Energy Fuels*, 2021, **5**, 52–78.

23 D. Unlu, O. Ilgen and N. D. Hilmioglu, *Chem. Eng. Res. Des.*, 2017, **118**, 248–258.

24 D. Unlu and N. Durmaz Hilmioglu, *Energy Fuels*, 2016, **30**, 2997–3003.

25 X. Kong, S. Wu, L. Liu, S. Li and J. Liu, *Mol. Catal.*, 2017, **439**, 180–185.

26 F. Gallucci, M. Van Sint Annaland and J. A. Kuipers, *Int. J. Hydrogen Energy*, 2010, **35**, 7142–7150.

27 J. M. Bermúdez, D. Beneroso, N. Rey-Raap, A. Arenillas and J. A. Menéndez, *Chem. Eng. Process.*, 2015, **95**, 1–8.

28 T. Flannelly, S. Dooley and J. J. Leahy, *Energy Fuels*, 2015, **29**, 7554–7565.

29 W. Zh. Weina, C. Chang, M. A. Chen and D. Fengguang, *Chin. J. Chem. Eng.*, 2014, **22**, 238–242.

30 C. Tao, L. Peng, J. Zhang and L. He, *Fuel Process. Technol.*, 2021, **213**, 106709.

31 Z. W. Wang, T. Z. Lei, L. Liu, J. L. Zhu, X. F. He and Z. F. Li, *BioResources*, 2012, **7**, 5972–5982.

32 T. Lei, Z. Wang, X. Chang, L. Lin, X. Yan, Y. Sun, X. Shi, X. He and J. Zhu, *Energy*, 2016, **95**, 29–40.

33 S. Lilonfe, I. Dimitriou, B. Davies, A. F. Abdul-Manan and J. McKechnie, *Chem. Eng. J.*, 2024, **479**, 147516.

34 C. Cañon, N. Sanchez and M. Cobo, *Data Brief*, 2022, **45**, 108681.

35 H. Liu, H. Meng, H. Cong, X. Shen, X. Chen, H. Xing and J. Dai, *RSC Adv.*, 2022, **12**, 34145–34153.

36 R. J. Wooley and V. Putsche, *Development of an ASPEN PLUS physical property database for biofuels components*, National Renewable Energy Lab (NREL), Golden, CO (United States), 1996.

37 J. De Riva, V. R. Ferro, D. Moreno, I. Diaz and J. Palomar, *Fuel Process. Technol.*, 2016, **146**, 29–38.

38 H. Ľudmila, J. Michal, Š. Andrea and H. Aleš, *Wood Res.*, 2015, **60**, 973–986.

39 G. Englmair, W. Kong, J. B. Berg, S. Furbo and J. Fan, *Appl. Therm. Eng.*, 2020, **166**, 114647.

40 R. Davis, L. Tao, E. C. Tan, M. J. Biddy, G. T. Beckham, C. Scarlata, J. Jacobson, K. Cafferty, J. Ross, J. Lukas and D. Knorr, *Process design and economics for the conversion of lignocellulosic biomass to hydrocarbons: dilute-acid and enzymatic deconstruction of biomass to sugars and biological conversion of sugars to hydrocarbons*, National Renewable Energy Lab (NREL), Golden, CO (United States), 2013.

41 A. Hasna, *J. Appl. Sci.*, 2011, **11**, 3613–3618.

42 H. Baum, T. Geissler and U. Westerkamp, *Z. für Verkehrswiss.*, 2009, **80**, 118.

43 F. Wu, Z. Zhou and A. L. Hicks, *Environ. Sci. Technol.*, 2019, **53**, 4078–4087.

44 J. Lin, S. Liu, Z. Han, R. Ma, C. Cui and S. Sun, *Chem. Eng. J.*, 2023, **452**, 139551.

45 H. S. Fogler, *Essentials of chemical reaction engineering*, Pearson Education, 2010.

46 R. Mannhold, H. Kubinyi and G. Folkers, *Molecular interaction fields: applications in drug discovery and ADME prediction*, John Wiley & Sons, 2006.

47 J. Zhou, W. Xu, Z. You, Z. Wang, Y. Luo, L. Gao, C. Yin, R. Peng and L. Lan, *Sci. Rep.*, 2016, **6**, 25149.

48 H. Goyal, A. Mehdad, R. F. Lobo, G. D. Stefanidis and D. G. Vlachos, *Ind. Eng. Chem. Res.*, 2019, **59**, 2516–2523.

49 M. Neubauer, T. Wallek and S. Lux, *Chem. Eng. Res. Des.*, 2022, **184**, 402–418.

50 J. Chaouki, S. Farag, M. Attia and J. Doucet, *Can. J. Chem. Eng.*, 2020, **98**, 832–847.

51 J. D. Moseley and C. O. Kappe, *Green Chem.*, 2011, **13**, 794–806.

52 A. Solouki, S. A. Jaffer and J. Chaouki, *Energy Rep.*, 2022, **8**, 4373–4385.

53 C. Zhuo, L. Xueqin, W. Zhiwei, Y. Yantao, S. Tanglei, H. Taoli, L. Peng, L. Yanling, W. Youqing, L. Tingzhou and Q. Jingshen, *Ind. Crops Prod.*, 2023, **192**, 116096.

54 L. Prasad, S. Pradhan, L. M. Das and S. N. Naik, *Appl. Energy*, 2012, **93**, 245–250.

55 T. Lei, Z. Wang, X. Chang, L. Lin, X. Yan, Y. Sun, X. Shi, X. He and J. Zhu, *Energy*, 2016, **95**, 29–40.

56 C. Sun, L. Chen, L. Zhai, H. Liu, K. Wang, C. Jiao and Z. Shen, *J. Clean. Prod.*, 2020, **277**, 123519.

57 M. Felix and S. H. Gheewala, *Int. J. Life Cycle Assess.*, 2014, **19**, 1424–1432.

58 Y. Lu, M. Shao, C. Zheng, H. Ji, X. Gao and Q. Wang, *Atmos. Environ.*, 2020, **231**, 117536.